

# Improving the radiative decay rate for dye molecules with hyperbolic metamaterials

J. Kim,<sup>1</sup> V. P. Drachev,<sup>1\*</sup> Z. Jacob,<sup>1,2</sup> G. V. Naik,<sup>1</sup> A. Boltasseva,<sup>1</sup> E. E. Narimanov,<sup>1</sup> and V. M. Shalaev<sup>1</sup>

<sup>1</sup>*Birck Nanotechnology Center and School of Electrical and Computer Engineering, Purdue University, West Lafayette, Indiana 47907, USA*

<sup>2</sup>*Department of Electrical and Computer Engineering, University of Alberta, Edmonton, AB T6G 2V4, Canada*  
[\\*vdrachev@purdue.edu](mailto:vdrachev@purdue.edu)

**Abstract:** We directly demonstrate an improvement in the radiative decay rate of dye molecules near multilayer hyperbolic metamaterials (HMMs). Our comprehensive study shows a radiative decay rate for rhodamine 800 (Rh800) that is several times higher due to the use of HMM samples as compared to dielectric substrates. This is also the first experimental demonstration that multilayer hyperbolic metamaterials provide an increase in the radiative decay rate relative to those from either thin or thick gold films.

©2012 Optical Society of America

**OCIS codes:** (160.3918) Metamaterials; (250.5403) Plasmonics; (250.5230) Photoluminescence.

---

## References and links

1. K. Drexhage, "Influence of a dielectric interface on fluorescence decay time," *J. Lumin.* **1**, 693–701 (1970).
2. W. Barnes, "Fluorescence near interfaces: the role of photonic mode density," *J. Mod. Opt.* **45**(4), 661–699 (1998).
3. G. Pake and E. Purcell, "Line shapes in nuclear paramagnetism," *Phys. Rev.* **74**(9), 1184–1188 (1948).
4. J. B. Khurgin, G. Sun, and R. A. Soref, "Enhancement of luminescence efficiency using surface plasmon polaritons: figures of merit," *J. Opt. Soc. Am. B* **24**(8), 1968–1980 (2007).
5. J. J. Burke, G. I. Stegeman, and T. Tamir, "Surface-polariton-like waves guided by thin, lossy metal films," *Phys. Rev. B Condens. Matter* **33**(8), 5186–5201 (1986).
6. E. H. Hellen and D. Axelrod, "Fluorescence emission at dielectric and metal-film interfaces," *J. Opt. Soc. Am. B* **4**(3), 337–350 (1987).
7. L. Luan, P. Sievert, W. Mu, Z. Hong, and J. Ketterson, "Highly directional fluorescence emission from dye molecules embedded in a dielectric layer adjacent to a silver film," *New J. Phys.* **10**(7), 073012 (2008).
8. G. Winter and W. L. Barnes, "Emission of light through thin silver films via near-field coupling to surface plasmon polaritons," *Appl. Phys. Lett.* **88**(5), 051109 (2006).
9. S. Hayashi, Y. Yamada, A. Maekawa, and M. Fujii, "Surface plasmon-mediated light emission from dye layer in reverse attenuated total reflection geometry," *Jpn. J. Appl. Phys.* **47**(2), 1152–1157 (2008).
10. H. Yoon, S. A. Maier, D. D. C. Bradley, and P. N. Stavrinou, "Surface plasmon coupled emission using conjugated light-emitting polymer films," *Opt. Mater. Express* **1**(6), 1127–1138 (2011).
11. R. M. Bakker, V. P. Drachev, Z. Liu, H. K. Yuan, R. H. Pedersen, A. Boltasseva, J. Chen, J. Irudayaraj, A. V. Kildishev, and V. M. Shalaev, "Nanoantenna array-induced fluorescence enhancement and reduced lifetimes," *New J. Phys.* **10**(12), 125022 (2008).
12. J. Khurgin, G. Sun, and R. Soref, "Electroluminescence efficiency enhancement using metal nanoparticles," *Appl. Phys. Lett.* **93**(2), 021120 (2008).
13. L. Novotny and B. Hecht, *Principles of nano-optics* (Cambridge University Press, 2006).
14. J. R. Lakowicz, "Radiative decay engineering 3. Surface plasmon-coupled directional emission," *Anal. Biochem.* **324**(2), 153–169 (2004).
15. K. Aslan, I. Gryczynski, J. Malicka, E. Matveeva, J. R. Lakowicz, and C. D. Geddes, "Metal-enhanced fluorescence: an emerging tool in biotechnology," *Curr. Opin. Biotechnol.* **16**(1), 55–62 (2005).
16. Z. Jacob, I. Smolyaninov, and E. Narimanov, "Broadband Purcell effect: Radiative decay engineering with metamaterials," Arxiv preprint arXiv:0910.3981 (2009).
17. Z. Jacob, "Classical and quantum optics of hyperbolic metamaterials," in *Dissertation* Purdue University, West Lafayette (2010).
18. Z. Jacob and E. E. Narimanov, "Optical hyperspace for plasmons: Dyakonov states in metamaterials," *Appl. Phys. Lett.* **93**(22), 221109 (2008).

19. S. M. Vukovic, I. V. Shadrivov, and Y. S. Kivshar, "Surface Bloch waves in metamaterial and metal-dielectric superlattices," *Appl. Phys. Lett.* **95**, 041902 (2009).
20. X. Ni, G. Naik, A. Kildishev, Y. Barnakov, A. Boltasseva, and V. Shalaev, "Effect of metallic and hyperbolic metamaterial surfaces on electric and magnetic dipole emission transitions," *Appl. Phys. B* **103**(3), 553–558 (2011).
21. Z. Jacob, J. Kim, G. Naik, A. Boltasseva, E. Narimanov, and V. Shalaev, "Engineering photonic density of states using metamaterials," *Appl. Phys. B* **100**(1), 215–218 (2010).
22. M. A. Noginov, H. Li, Y. A. Barnakov, D. Dryden, G. Nataraj, G. Zhu, C. E. Bonner, M. Mayy, Z. Jacob, and E. Narimanov, "Controlling spontaneous emission with metamaterials," *Opt. Lett.* **35**(11), 1863–1865 (2010).
23. M. D. Escarra, S. Thongrattanasiri, A. J. Hoffman, J. Chen, W. O. Charles, K. Conover, V. A. Podolskiy, and C. F. Gmachl, "Broadband, Low-Dispersion, Mid-Infrared Metamaterials," in *Quantum Electronics and Laser Science Conference*, OSA Technical Digest (CD) (Optical Society of America, 2010), paper QWB4.
24. K. Selanger, J. Falnes, and T. Sikkeland, "Fluorescence lifetime studies of Rhodamine 6G in methanol," *J. Phys. Chem.* **81**(20), 1960–1963 (1977).
25. A. Penzkofer and Y. Lu, "Fluorescence quenching of Rhodamine 6G in methanol at high concentration," *Chem. Phys.* **103**(2-3), 399–405 (1986).
26. F. Ammer, A. Penzkofer, and P. Weidner, "Concentration-dependent fluorescence behaviour of oxazine 750 and rhodamine 6G in porous silicate xerogel monoliths," *Chem. Phys.* **192**(3), 325–331 (1995).
27. R. M. A. Azzam and N. M. Bashara, *Ellipsometry and polarized light* (North Holland, 1987).
28. S. M. Rytov, "Electromagnetic properties of a finely stratified medium," *Sov. Phys. JETP* **2**, 466–475 (1956).
29. B. Wood, J. Pendry, and D. Tsai, "Directed subwavelength imaging using a layered metal-dielectric system," *Phys. Rev. B* **74**(11), 115116 (2006).
30. O. Kidwai, S. V. Zhukovsky, and J. E. Sipe, "Dipole radiation near hyperbolic metamaterials: applicability of effective-medium approximation," *Opt. Lett.* **36**(13), 2530–2532 (2011).
31. A. P. Vinogradov, A. I. Ignatov, A. M. Merzlikin, S. A. Tretyakov, and C. R. Simovski, "Additional effective medium parameters for composite materials (excess surface currents)," *Opt. Express* **19**(7), 6699–6704 (2011).
32. K. Aslan, Z. Leonenko, J. R. Lakowicz, and C. D. Geddes, "Annealed silver-island films for applications in metal-enhanced fluorescence: interpretation in terms of radiating plasmons," *J. Fluoresc.* **15**(5), 643–654 (2005).
33. M. Noginov, G. Zhu, M. Bahoura, C. Small, C. Davison, J. Adegoke, V. P. Drachev, P. Nyga, and V. Shalaev, "Enhancement of spontaneous and stimulated emission of a rhodamine 6G dye by an Ag aggregate," *Phys. Rev. B* **74**(18), 184203 (2006).
34. Y. Zhang, K. Aslan, S. N. Malyn, and C. D. Geddes, "Metal-enhanced phosphorescence (MEP)," *Chem. Phys. Lett.* **427**(4-6), 432–437 (2006).
35. A. T. R. Williams, S. A. Winfield, and J. N. Miller, "Relative fluorescence quantum yields using a computer-controlled luminescence spectrometer," *Analyst (Lond.)* **108**(1290), 1067–1071 (1983).
36. D. P. Benfey, D. C. Brown, S. J. Davis, L. G. Piper, and R. F. Foutter, "Diode-pumped dye laser analysis and design," *Appl. Opt.* **31**(33), 7034–7041 (1992).
37. H. N. S. Krishnamoorthy, Z. Jacob, E. Narimanov, I. Kretzschmar, and V. M. Menon, "Metamaterial based broadband engineering of quantum dot spontaneous emission," arXiv:0912.2454v1 [physics.optics] (2009).
38. G. Ford and W. Weber, "Electromagnetic interactions of molecules with metal surfaces," *Phys. Rep.* **113**(4), 195–287 (1984).
39. A. N. Poddubny, P. A. Belov, and Y. S. Kivshar, "Spontaneous radiation of a finite-size dipole emitter in hyperbolic media," *Phys. Rev. A* **84**(2), 023807 (2011).

## 1. Introduction

When a mirror is placed near a fluorescing molecule, both the angular distribution and the decay time of the fluorescence are affected. This occurs because part of the emitted light wave is reflected by the metal or dielectric mirror and interferes with the non-reflected part [1]. This also may result in changes in the non-radiative decay rate of the fluorescence due to the fact that the excited molecules may lose energy to the interface via non-radiative energy transfer.

The rate of spontaneous emission is proportional to the local photonic density of states (PDOS), according to Fermi's golden rule. The photonic density of states in a material can be modified due to the interference of emitted and reflected waves [2]. In the case of destructive interference, the environment does not support emission, and the PDOS is low. Non-radiative decay can be modified due to dipole-image interaction and excitation of the surface-plasmon polaritons or wave-guiding modes [2]. The modification of spontaneous emission with a planar interface is of the same origin as that suggested by Purcell, who pointed out that the PDOS and consequently the radiative decay rate can be changed in a cavity-emitter hybrid system [3]. After the pioneering experiments by Drexhage and co-authors summarized in [1], a large number of theoretical and experimental studies on the modification of spontaneous

emission have been performed. The inherent limitations of molecular fluorescence detection due to quantum yield, auto-fluorescence, and photostability have led to the development of PDOS engineering that uses metal-dielectric interfaces [2,4], metal-film interfaces [5–10], nanostructures [11], and particles [12].

It follows from the surface-plasmon polariton (SPP) dispersion relation that the wavevector component along the interface is always larger than the wavevector of light in free space for a given energy [13]. Consequently, this means that the excitation of SPPs by light on a planar interface is only possible if a wavevector component of the exciting light can be increased over the free space value. Fluorescence studies typically employ the conceptually simplest way to excite an SPP by placing fluorophores, embedded in a solid or liquid matrix with a refractive index more than unity, in the vicinity of the interface [14,15]. Surface plasmon-coupled emission from the fluorophores then results in an angular distribution of photoluminescence that is directional [5–10].

The emission rate can be considerably altered for a point dipole placed inside a hyperbolic metamaterial (HMM) with  $\epsilon = \text{diag}(\epsilon_x, \epsilon_y, \epsilon_z)$ , where  $\epsilon_x = \epsilon_y < 0$  and  $\epsilon_z > 0$ , due to the large expected density of states [16–18]. The dispersion relation  $\omega^2/c^2 = k_x^2/\epsilon_x + k_z^2/\epsilon_z$  becomes hyperbolic in the case of different signs of the permittivity components (here the wavevector is always selected to be in the xz plane). This type of metamaterials has been previously considered for various applications [19,20]. Such materials can be obtained by creating a multilayer, metal-dielectric composite [21] or a nanorod array structure [22]. The theory [16–18] predicts that the photonics density of states can be much larger for fluorophores in the vicinity of HMM relative to conventional materials. The Purcell factor, which is the ratio of the radiative decay rate of the molecules with HMM and in the free space, is also predicted to be much higher for HMM and spectrally broadband [16–18]. However this theory does not take into account effect of the nonradiative decay rate and the existing experiments on fluorophores with HMMs did not include measurements of the radiative decay rate [21,22]. We will show below that the effect of HMM on the nonradiative rate is quite strong and cannot be neglected for conclusive results.

Indeed, similar to SPP, the limiting factor of the radiative decay is in the out-coupling of the HMM modes to the low PDOS of free space [4]. The PDOS in an SPP mode can be quite high, mostly due to the low group velocity, and thus Purcell factors of about  $10^3$  are realistic. However, the use of an SPP mode does not necessarily help to overcome the problem of the low free-space density of states. Since the radiation modes near a metal surface are different than those of free space (the radiation modes must be orthogonal to the SPP modes), radiative coupling into the radiation mode must compete with the non-radiative mode of the SPP itself [4].

In this work, we have studied the modification of spontaneous emission from a fluorophore placed in the vicinity of a hyperbolic metamaterial. As it is mentioned above the most interesting aspect of such metamaterials is the broad spectral range in which hyperbolic dispersion exists. In initial studies, researchers reported changes in the overall lifetime of a molecule's excited state near the surface of HMMs [21–23]. However, to clearly demonstrate the effect of HMMs on molecules, the radiative decay rate should be measured separately, which was not done in [21–23]. In this work, we demonstrate an increase in the radiative decay rate for a rhodamine 800 dye layer placed in the vicinity of an HMM structure by measuring the apparent quantum yield, absorption, emission, reflection, and lifetime of the dye molecules. We also compare the radiative decay rate with control samples that are similar to those used in classic experiments, namely thin and thick gold films. We also study the effect of the distance between the dye molecules and various kinds of substrates. Finally, we show that both our gold-film control samples as well as our experimental samples can be theoretically considered as having an effective layer with hyperbolic dispersion. Intuitively, this result follows from the close similarity between the permittivities of an HMM and the

criteria for an SPP mode to exist at a metal (m) and dielectric (d) interface, namely  $\text{Re}(\epsilon_m) < 0$  and  $|\text{Re}(\epsilon_m)| > \epsilon_d$ . All the samples can also support directional emission as a result of the excitation of an SPP at the metal-film interfaces. In fact, any layer containing a metal-dielectric can be effectively represented by a layer with hyperbolic dispersion, as we demonstrate below.

## 2. Experiment

### 2.1 Sample fabrication

Our multilayer HMM samples consisted of 16 stacked layers of gold (Au) and alumina ( $\text{Al}_2\text{O}_3$ ) on a glass substrate, as shown in Fig. 1(a). The alternating gold and alumina layers were deposited sequentially using an electron-beam vacuum evaporator. The layer thicknesses are each 19 nm, which is deeply subwavelength for our experiments. The layer has a refractive index of 1.61 at a wavelength of 633 nm, as determined by ellipsometry. After the deposition of the eight gold and eight alumina layers, the total thickness of the HMM was 302 nm. On top of the uppermost gold layer, a very thin dielectric spacer layer composed of epoxy (SU-8 2000.2 or SU-8 2000.5 at 9.4% weight diluted with SU-8 2000 thinner) was spin coated. Two substrates for each sample type were fabricated with different spacer layer thicknesses of  $h_d = 21 \pm 3$  nm and  $h_{up} = 89 \pm 5$  nm, as determined by atomic force microscopy (AFM, Dimension 3100, Veeco) and surface profilometry (Alpha-Step IQ, KLA-Tencor). The thickness of the epoxy layer was controlled by the dilution ratio between the SU-8 2000.2 and the SU-8 2000 thinner and the spin speed. The epoxy layer had a refractive index of 1.52 at 633 nm, which is similar to that of alumina. Finally, a 21-nm dye thin film of epoxy mixed with rhodamine 800 (Rh800) at a 100  $\mu\text{M}$  concentration was spin coated on top of the spacer layer, as shown in Fig. 1(b). For comparison purposes, two control samples were also fabricated; these consisted of thick (300 nm) and thin (20 nm) gold layers, respectively. In addition, a reference dye thin film was prepared on a bare glass substrate.

### 2.2 Choice of spacer and thin dye layers

The thickness of the thin dye/epoxy layer was carefully controlled by the spin speed and the dilution ratio. The rough thickness was determined by the ratio between SU-8 2000.2 or

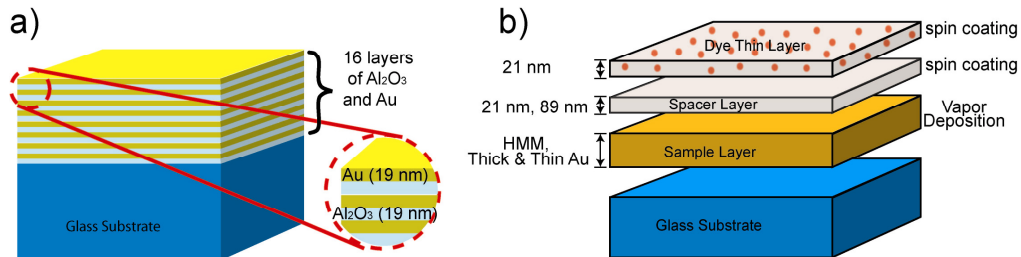


Fig. 1. (a) The planar, stacked HMM structure with 19-nm alumina and 19-nm gold layers. The total thickness is 302 nm. (b) Illustration of the dye thin film with HMM layers, a thick gold layer (300 nm), and a thin gold layer (20 nm). Another reference sample was also prepared with only a dye thin film on a glass substrate.

SU-8 2000.5 and the SU-8 thinner. For relatively thin films, a 1:5 ratio of SU-8 2000.2 to SU-8 thinner was usually sufficient. When a ratio higher than 1:5 was used, the epoxy molecular weight was too low, and the resultant film exhibited a refractive index that was different from a normal epoxy film. Fine control over the layer thickness was obtained by controlling the spin speed. The spin speed was limited to no more than 5000 rpm, and hence the minimum achievable film thickness by diluting and using the maximum spin speed was 21 nm. With this method, we were able to vary the thickness in steps of 5 to 10 nm with only a

10% error. Overall, the thickness of the spacer layer in the range of 21 nm to 89 nm was chosen. A heating process was required after spin coating the epoxy and dye-epoxy solution in order to remove the residual solution and solidify the film.

The dye concentration in the thin film affects the dye/epoxy film parameters. Previous studies have shown that the lifetime and quantum efficiency of fluorophores depend on the molecular concentration and are usually higher in lower molecular concentrations [24–26]. At high concentrations above  $10^{-2}$  M, the fluorescence lifetime in solution is rapidly reduced due to quenching processes such as concentration quenching and fast non-radiative de-excitation channels. At low concentrations, the fluorescence lifetime is independent of concentration [25]. In thin films of rhodamine 800 embedded in an epoxy matrix, the quantum yield of the dye gradually increases with decreasing concentration, as shown in Table 1. In our experiments, we chose a 100  $\mu$ M concentration to avoid concentration quenching and to obtain better performance with a higher quantum yield. Additionally, the experimental parameters such as heating temperature and time, laser exposure time, and power also affected the properties of the dye thin film. Therefore, the experimental conditions for all samples and measurements in our studies were carefully adjusted.

### 2.3 Retrieval of effective optical parameters

As mentioned above, all the samples containing a metal-dielectric interface can be considered to have an effective layer that is anisotropic with hyperbolic dispersion. The dispersion relations for the effective permittivities of our samples are shown in the Appendix and Table 2 for an excitation wavelength of 633 nm and a luminescence wavelength of 720 nm. To retrieve these optical parameters, we first simulated layered structures similar to the fabricated samples and compared the experimental and simulated reflection spectra for six metal-containing samples including thick Au films, thin Au films, and the multilayer structure. The only differences between the simulated structures and the experimental samples were fine adjustments of the layer thicknesses due to the discretization of the simulation domain. The experimental reflection spectra and our simulation results are shown in Fig. 2(a) – Fig. 2(c). Second, we simulated the transmission and reflection spectra at different angles for the fabricated structures. Finally, these spectra were fitted with model structures containing effective layers as shown in the Appendix. The simulations for the experimental and the effective, stratified, planar structures were performed with ellipsometry software (W-VASE, J. A. Woollam Co., Inc.) that is based on a 4x4 scattering-matrix method for solving Maxwell's Eq [27]. For the model-layer dispersion calculations, the Rytov effective medium theory is employed [28]. The effective parameters for a multilayer, periodic structure with a period  $d = b + a$  and containing both a metal (with permittivity  $\epsilon_2$  and permeability  $\mu_2$ ) and a dielectric ( $\epsilon_1, \mu_1$ ) are given below.

**Table 1. Quantum Yield Versus Concentration of Rh800 in Epoxy Films**

Concentration	Quantum yield
100 $\mu$ M	0.138
500 $\mu$ M	0.0769
1 mM	0.0312

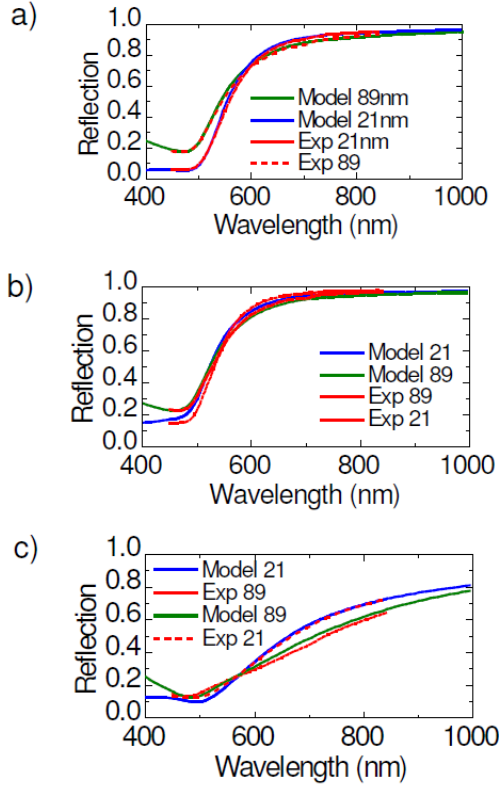


Fig. 2. Measured (exp) and calculated (model) reflection spectra for three different thin-film samples: (a) Thin Au films with 21-nm and 89-nm spacers. (b) 300 nm Au films with 21-nm and 89-nm spacers. (c) Multilayer (HMM) films with 21-nm and 89-nm spacers.

In the case of light propagating perpendicular to the layers, the effective permittivity (x-component) and permeability are [28]:

$$\varepsilon_{eff} = \bar{\varepsilon} \left( 1 - \frac{ikab}{4d} \frac{\mu_1 \varepsilon_2 - \mu_2 \varepsilon_1}{\sqrt{\bar{\varepsilon} \bar{\mu}}} \right), \quad (1)$$

$$\mu_{eff} = \bar{\mu} \left( 1 + \frac{ikab}{4d} \frac{\mu_1 \varepsilon_2 - \mu_2 \varepsilon_1}{\sqrt{\bar{\varepsilon} \bar{\mu}}} \right), \quad (2)$$

$$\bar{\varepsilon} = \left( \frac{b\varepsilon_2 + a\varepsilon_1}{a+b} \right); \bar{\mu} = \left( \frac{b\mu_2 + a\mu_1}{a+b} \right). \quad (3)$$

**Table 2. Effective permittivities for interface-containing layers. HMM-21: a 275-nm thickness (model 20), HMM-89: a 240-nm thickness (model 24), Thin Au-21: a 34-nm thickness (model 23), and 300 nm Au-21: a 53-nm thickness (model 21). The model details are described in the Appendix.**

	HMM-21	HMM-89	Thin Au-21	300 nm Au-21
$\varepsilon_x$ (at 632 nm)	-5.8+i1.1	-6.6+i1.1	-5.6+i0.9	-12.54+i1.7
$\varepsilon_z$ (632 nm)	8.3+i0.35	10.2+i0.7	7+i0.5	2.8+i0.09
$\varepsilon_x$ (720 nm)	-9.9+i1.1	-10.8+i1.1	-9.2+i0.9	-15.5+i1.6
$\varepsilon_z$ (720 nm)	7.4+i0.12	8.6+i0.2	6+i0.15	2.6+i0.03

In the case of light propagating parallel to the layers, the effective permittivity (z-component) is:

$$\epsilon_{eff} = \tilde{\epsilon}; \tilde{\epsilon}^{-1} = \frac{a/\epsilon_1 + b/\epsilon_2}{a+b}. \quad (4)$$

Corrections are of the order of  $(kd)^2$  in this case. Note that the Rytov correction for the perpendicular propagation describes a magnetic response on the order of  $(kd)$ . Details of the model parameters including the fitting thicknesses  $a$  and  $b$  can be found in the Appendix. We note that all the samples are hyperbolic, as shown in Table 2. The differences between the samples are in the hyperbolic layer thicknesses and in their compositions, particularly in the case of the thick Au film, since the interface layer occupies a comparatively smaller volume. It is worth mentioning that the introduction of average fields and effective parameters makes sense if  $kd|n| \ll 1$ , where  $n$  is the effective refractive index. This condition is fulfilled for  $d \ll 35$  nm for our samples. We also note that the effective parameters here just illustrate the tendencies in the films and cannot completely describe the system. That is the reason why both the transmission and reflection spectra can be fitted only for effective-layer thicknesses that are 10-20% lower than the experimental values. It was shown previously [29,30] that increasing the number of layers at the same thickness brings the results for the multilayer structure closer and closer to those of a homogeneous sample. The Rytov theory is further developed in [31] by introducing additional effective parameters for the excess surface currents. In applying this approach, however, we must still fulfill the subwavelength condition above. The experimental design in our case has an intermediate period that is comparable to the wavelength in material. To simplify our further discussions, we have included the reflection and transmission values for the  $p$  polarization at two wavelengths of interest in Table 3 and in more detail spectra in the Appendix.

#### 2.4 Optical Detection

We measured the fluorescence spectra of our samples with a 633-nm excitation wavelength and a power of 0.53  $\mu$ W. The spectra were collected using two objectives (50x, NA 0.75 or 50x, NA 0.45) and a spectrometer (Renishaw). The power transmission and reflection spectra of dye thin films on the HMM substrates, the gold substrates, and the bare glass substrates were recorded at room temperature with a commercial UV-Vis-NIR spectrophotometer (Lambda 950, Perkin Elmer). For quantum yield measurements, the dye

**Table 3. Reflection, Transmission and Absorption Data in % for Selected Samples under P-polarized Light at 633 nm and 720/715 nm and Various Incidence Angles**

	pR_632nm	pR_720/715	pT_632	pT_720	pA_632	pA_720
HMM-89 0°, 40°	80	90	0.1		20	10
HMM-89 80°	93.5	96	0.04		6.5	4
ThinAu-89 0°, 40°	36	49/48.5	49	39/40	15	11.5

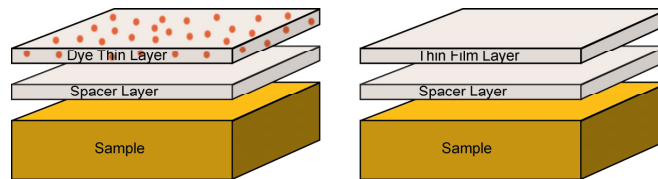


Fig. 3. Sample schematic for absorption measurements. Two identical samples were prepared with dye (left) and without dye (right) in the epoxy thin film layer for each type of sample (HMM, thick and thin gold, and bare glass samples).

film absorption spectrum has to be collected while excluding the structure's absorption. Therefore, an identical pair of substrates was prepared for all samples except for the existence of dye molecules in the top layer for one sample in the pair (see Fig. 3). The dye absorption spectra are shown in Fig. 4. The absorption spectra are calculated from the transmission ( $T$ ) and reflection ( $R$ ) spectra as  $A = 1 - (T + R)$ . The dye absorption is obtained then by subtracting the absorption of the twin sample without dye.

Lifetime measurements were performed with a time-correlated single-photon counting board (Timeharp 200, Picoquant) for data acquisition and a single-photon avalanche diode (SPAD) as a detector. The dye thin film was excited by a pulsed diode laser with a pulse duration of 88 ps, a wavelength of 635 nm, and a repetition rate of 20 MHz. A light beam carrying 0.28  $\mu\text{W}$  of power was focused onto the sample using an objective lens (50x, NA 0.75, Olympus). The fluorescence light emitted by the dye was collected with the same objective lens. The excitation light was blocked by a dichroic mirror and a long-pass filter to reject any remaining scattered laser light. The fluorescence light passed through a small aperture to enable confocal detection and was directed to the small detection area of the SPAD (SPCM-AQR-13, Perkin Elmer). The intensity decay curves were de-convolved from the instrument response function (IRF) and then fitted by a mono- or multi-exponential decay function.

### 3. Results and analysis

Different environments near the dye molecules strongly influence the absorption and fluorescence spectra as well as internal molecular properties such as quantum yield, radiative and non-radiative decay rates. We investigated these effects for all samples and with two different spacer thicknesses of 21 and 89 nm. The changes in the absorption spectra are clearly seen in Fig. 4. Table 4 shows the absorption and lifetime results for both spacer thicknesses and for each type of sample. At the 89-nm spacer thickness, absorption is enhanced approximately 8 times for both thick and thin gold substrates and about 5.5 times for the HMM substrate, compared to the bare glass substrate. For the 21-nm spacer layer samples, the enhancements are about 3.5 for the gold and 2.5 for the HMM substrates.

Changes in molecular absorption near a metallic surface have been observed for plasmonic nanostructure in previous studies [32–34]. It was also observed that the enhanced absorption can directly result in surface-enhanced luminescence phenomena, such as metal-enhanced fluorescence [14, 15, 33] and metal-enhanced phosphorescence [34].

Figure 5 shows the photoluminescence (PL) spectra our samples for both spacer layers. As shown in Fig. 5, the PL signal for the 89-nm spacer layer is about 9.3 times stronger for both the HMM and the thick gold substrates (compared to the bare glass substrate), while the thin gold film provides about 6.4 times enhancement. These PL enhancement values are different from the absorption values in that the highest absorption values are observed in the

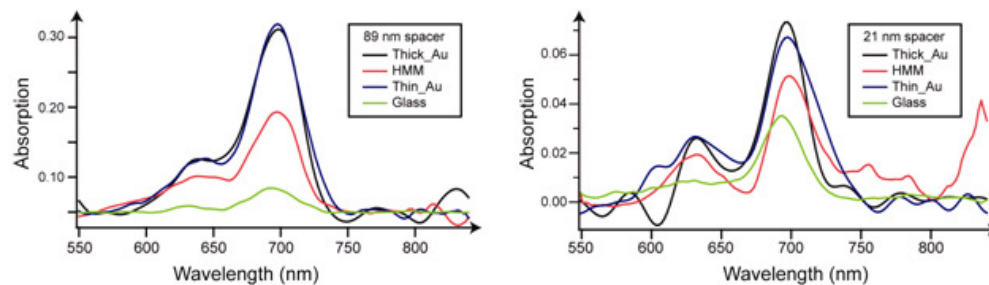


Fig. 4. Absorption (%) spectra of dye molecules in an epoxy layer for the samples under study.

**Table 4. Absorption at 633 nm and Total Lifetime Results for Different Substrates and for Both Spacer Layers**

	Absorption (%)		Lifetime (ns)	
	89 nm	21 nm	89 nm	21 nm
HMM	0.0485	0.0187	1.66	1.62
Thick Au	0.0706	0.0258	1.80	2.09
Thin Au	0.0689	0.0265	1.62	1.44
Glass	0.0089 7	0.00753	2.21	2.18

thick and thin gold substrates (see Table 4) rather than in the HMM sample. The highest PL enhancements are obtained for the multilayer HMM and the thick gold sample, but the strongest absorption appears in the thick and thin gold samples. This indicates that the dye molecules on the HMM sample are more efficiently radiative with less absorption than on other control samples.

The values of the fluorescence quantum yield,  $Q_s$ , of the dye thin film on the bare glass substrates without HMM or gold layers were evaluated by using the reference method [35]:

$$Q_s = Q_{ref} \cdot \frac{A_{ref}}{A_s} \cdot \frac{I_s}{I_{ref}} \cdot \left( \frac{n_s}{n_{ref}} \right)^2, \quad (5)$$

where  $Q_{ref}$  is the quantum yield of the reference,  $A$  is the absorption,  $I$  is the integrated fluorescence intensity, and  $n$  is the average refractive index. The subscripts  $s$  and  $ref$  refer to the sample and the reference, respectively. Here, Rh800 in methanol served as the reference, and its quantum yield is 0.086 [36].

Two important parameters, namely the quantum yield and the lifetime, are related as follows:

$$Q = \Gamma_r \tau; \quad \tau = [\Gamma_r + \kappa_{nr}]^{-1} = \Gamma^{-1}. \quad (6)$$

Here,  $\Gamma_r$  is the radiative decay rate,  $\kappa_{nr}$  is the non-radiative decay rate,  $\tau$  is the excited state lifetime, and  $\Gamma$  is the total decay rate. Equation (6) states that an increase in the ratio of the

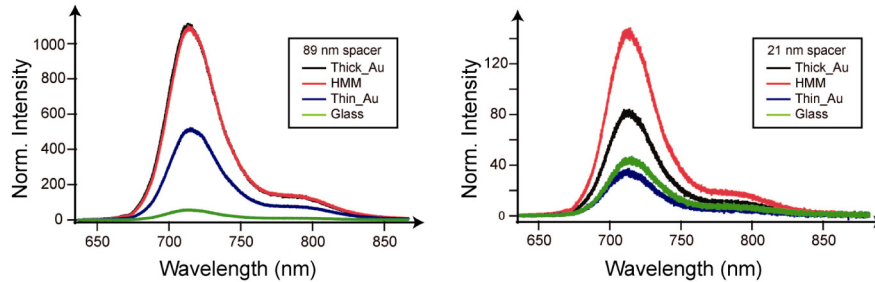


Fig. 5. Fluorescence spectra for the samples for both the 89-nm and 21-nm spacer layers.

**Table 5. Experimental Values Normalized by Those of the Glass Substrate, and the Apparent Radiative Decay Rates**

	Fluorescence ratio		Absorption ratio		Lifetime ratio		$(\Gamma_r)_{sample}/(\Gamma_r)_{ref}$	
	89 nm	21 nm	89 nm	21 nm	89 nm	21 nm	89 nm	21 nm
HMM	9.3	1.6	5.41	2.48	0.75	0.74	2.3	0.86
Thick Au	9.4	0.9	7.87	3.43	0.81	0.96	1.5	0.28
Thin Au	6.4	0.55	7.68	3.52	0.73	0.66	1.13	0.24

radiative and non-radiative decay rates will result in an increase of the quantum yield. Direct measurements of both the lifetime and the quantum yield changes are necessary for

conclusive results on the radiative decay rate. The quantum yield is simply the ratio of the emitted to the absorbed photons. By using the reference method, the quantum yield can be experimentally obtained through absorption and fluorescence measurements for the samples under study relative to the corresponding dye/epoxy reference sample (see Eq. (5)). The apparent quantum yield then can be determined by that of the reference sample through Eq. (5). Thus we can find the apparent radiative decay rate directly from experimental data through:

$$\frac{(\Gamma_r)_s}{(\Gamma_r)_{ref}} = \frac{\tau_{ref}}{\tau_s} \cdot \frac{A_{ref}}{A_s} \cdot \frac{I_s}{I_{ref}} \cdot \left( \frac{n_s}{n_{ref}} \right)^2, \quad (7)$$

where  $I_s$  and  $I_{ref}$  are the total integrated intensities from the PL signal, and  $A_s$  and  $A_{ref}$  the absorption values at the excitation wavelength of the dye thin film, for the samples and glass substrates, respectively. From the comprehensive measurements and the experimental results, including emission lifetime, we obtained the apparent radiative decay rate of the dye thin film on top of the HMM and the thin and thick gold substrates after normalizing with those of the corresponding glass substrates (see Table 5). Note that the dye emission directed oppositely to the detection direction can be approximately taken into account through the transmission parameter  $(1 + T)$ . The use of the transmission-parameter estimate provides a good agreement with emission simulations for thin gold films about 20 nm thick and bare glass substrates [6, 7].

Since the apparent quantum yields of the dye molecules on glass substrates were directly measured (see Table 1) to be 0.138 at a 100- $\mu$ M concentration, in Table 6 we directly evaluate the radiative decay rates, the non-radiative decay rates, and the ratios of these values to those of the reference (glass) substrates. We also calculate these values and the apparent quantum yields using Eq. (5) and Eq. (6) for the sample substrates (see Table 6). The enhancements of the PL intensity measured using two objectives with NA = 0.45 or NA = 0.75 are approximately equal, which means that the central part of the angular PL distribution does not change much for our samples relative to the glass substrate. Note that the objectives do not collect the sharp peaks in the pattern occurring at the critical angle for bare glass and at the surface-plasmon angle for metal-coated glass. The peak at the critical angle can be collected with an objective of numerical aperture  $NA > n_1 = \varepsilon_1^{1/2}$ . The surface-plasmon peak will be collected if  $NA > \text{Re}[(\varepsilon_1 \varepsilon_2 / \varepsilon_1 + \varepsilon_2)^{1/2}]$ , where  $\text{Re}(\varepsilon_2) < 0$  and  $|\text{Re}(\varepsilon_2)| > \varepsilon_1$  for a surface plasmon to exist at the 1-2 interface. Typically the NA should be greater than 1.4 to collect these peaks [6].

Note that the total dye-emitted power for the reference glass (and for the thin gold film as well) is estimated from our measurements and the literature data for a collection ratio from both sides of the substrate. For the highly reflective samples, however, since the SPP peak is typically out the range of the collection objective, our data for the apparent radiative decay rates and quantum yields represent a lower bound.

**Table 6. Radiative and Non-radiative Decay Rates, the Ratio Between Them, and the Quantum Yields for the Reference Sample (Glass Substrate), the HMM Sample, and the Thick and Thin Gold Samples**

	$\Gamma_r$ ( $s^{-1}$ ) $\times 10^{-8}$		$k_{nr}$ ( $s^{-1}$ ) $\times 10^{-8}$		$\Gamma_r/k_{nr}$		Q	
	89 nm	21 nm	89 nm	21 nm	89 nm	21 nm	89 nm	21 nm
HMM	1.4	0.54	4.6	5.66	0.3	0.095	0.23	0.09
Thick Au	0.9	0.18	4.6	4.6	0.2	0.04	0.17	0.038
Thin Au	0.7	0.15	5.5	6.8	0.13	0.02	0.12	0.02
Glass, ref	0.62	0.63	3.9	3.96	0.16	0.16	0.14	0.14

#### 4. Discussion

From the results above, we clearly see that the HMM substrates provide a more efficient radiative mechanism than the other control samples, as confirmed by all the representative data such as the radiative decay rates and the quantum efficiencies.

Several optical phenomena occur at metal surfaces, with each being important at a particular range of distances between the fluorophore and the interface. At distances longer than visible wavelengths, interference between the propagating, emitted light and its reflection dominates. At the intermediate ranges studied here, the evanescent near field of the dipole excites propagating surface plasmons, and a partial transfer of energy into heat occurs due to losses in metal. At very close ranges, the energy transfer into electron-hole pairs may become significant.

Interestingly, all of our samples show a decrease in the dye absorption for the thin spacer thickness  $h_d$  relative to the thick one  $h_{up}$  by the same factor of about 2.6-2.7, which indicates that the same mechanism is involved in the absorption enhancement for all the thin-spacer samples. Our analysis shows that this is a result of interference of the incident and reflected fields. Indeed, the absorption power for a molecule under light incident with a field amplitude of  $E$  is [13]:

$$P_{abs} = \frac{\omega}{2} \text{Im}\{\alpha\} \left\langle \left| \mathbf{n}_\mu \cdot \mathbf{E} \right|^2 \right\rangle = \frac{\omega}{6} \text{Im}\{\alpha\} |\mathbf{E}|^2, \quad (8)$$

where  $\mathbf{n}_\mu$  is the unit vector in the direction of dipole  $\boldsymbol{\mu}$ ,  $\omega$  is the light frequency,  $\alpha$  is the molecule polarizability, and the orientational average is used to account for the isotropic angular distribution of the dipoles. Thus, the absorption ratio for a dye layer at a distance  $h_{up}$  to that at  $h_d$  with a wavevector  $k_1$  directed normal to the interface can be written as:

$$\frac{P_{abs}(h_{up})}{P_{abs}(h_d)} = \frac{|\mathbf{E}(h_{up})|^2}{|\mathbf{E}(h_d)|^2} = \frac{1 + |r|^2 + 2|r|\cos(\beta + 2k_1 h_{up})}{1 + |r|^2 + 2|r|\cos(\beta + 2k_1 h_d)}. \quad (9)$$

The amplitude reflection coefficient  $r$  is given by

$$r = |r| \exp(i\beta) = \frac{n_1 - n_2 - i\kappa_2}{n_1 + n_2 + i\kappa_2}, \quad (10)$$

where  $n_1$  and  $n_2 + i\kappa_2$  are the refractive indices of the epoxy layer and the sample, respectively. The sign convention of the field phase factor is  $\exp i(kz - \omega t)$ , and  $\beta$  is the phase shift of the reflected field. The phase shift can be calculated from the known refractive indices:

$$\tan(\pi + \beta) = \frac{2\kappa_2 n_1}{n_2^2 + \kappa_2^2 - n_1^2}. \quad (11)$$

The phase shift  $\beta$  is selected to be in the third quadrant due to the fact that both  $\text{Re}(r)$  and  $\text{Im}(r)$  are negative. We calculate that  $\beta \approx -2.34$  for the 300-nm Au film and  $\beta_{HMM} \approx -2.08$  for the multilayer sample. Thus, we observe a reasonable correspondence for the Au film:  $P_{abs}(90\text{nm})/P_{abs}(20\text{nm}) \approx 2.34 \pm 0.3$  versus 2.7 for the experimental ratio. It confirms that the changes in absorption can be explained by the interference of the incident and reflected waves. Another observation is that the ratio (9) for the HMM sample is about  $1.65 \pm 0.2$ , compared to 2.6 from the experiments, which indicates a poor agreement between the effective parameters of the HMM and 8-period multilayer structure. The same

conclusion can be made from the calculated absorption ratio between the thick gold and multilayer samples:  $P_{abs}^{Au300}(90nm)/P_{abs}^{HMM}(90nm) \approx 1.06$ , which is less than the experimental value of 1.45. This poor agreement gives an additional, quantitative confirmation that the effective-medium description is not sufficiently accurate in terms of the phase shift of the reflected wave. This is really no surprise, since the geometrical penetration depth calculated from the effective parameters is  $L = \beta\lambda/4\pi\kappa_2 \approx 20\text{nm}$  and is less than the period of the multilayer structure.

The changes in the PL intensity require a more complicated analysis. The energy dissipation rate is defined through the total dipole field at the dipole origin. This field is a sum of the primary dipole field and the field reflected from the planar structure [13]:

$$P = \frac{dW}{dt} = \frac{\omega}{2} \text{Im}\{\boldsymbol{\mu}^* \cdot \mathbf{E}(\mathbf{r}_0)\}, \quad (12)$$

$$\frac{P}{P_0} = 1 + \frac{6\pi\epsilon_0\epsilon}{|\boldsymbol{\mu}|^2} \frac{1}{k^3} \text{Im}\{\mathbf{u}^* \cdot \mathbf{E}_r(\mathbf{r}_0)\}, P_0 = \frac{|\boldsymbol{\mu}|^2}{12\pi} \frac{\omega}{\epsilon_0\epsilon} k^3. \quad (13)$$

The power spectra presented in Fig. 6 are calculated as follows [37]:

$$\Delta P_{prop}(u_{prop})/P_0 = (3/2)Qk_1^{-3} \text{Re}(I_{prop}) \quad (14)$$

$$I_{prop} = \frac{e^{2it_{prop}d}}{|\boldsymbol{\mu}|^2} \left[ \mu_{\perp}^2(k_1^2 - t_{prop}^2)r_p(u_{prop}) + 0.5\mu_{\parallel}^2k_1^2r_s(u_{prop}) - 0.5\mu_{\parallel}^2t_{prop}^2r_p(u_{prop}) \right] \quad (15)$$

$$\Delta P_{ev}(u_{ev})/P_0 = (3/2)Qk_1^{-3} \text{Re}(I_{ev}) \quad (16)$$

$$I_{prop} = \frac{e^{2it_{prop}d}}{|\boldsymbol{\mu}|^2} \left[ \mu_{\perp}^2(k_1^2 - t_{prop}^2)r_p(u_{prop}) + 0.5\mu_{\parallel}^2k_1^2r_s(u_{prop}) - 0.5\mu_{\parallel}^2t_{prop}^2r_p(u_{prop}) \right] \quad (17)$$

$$I_{ev} = \frac{e^{-2t_{ev}d}}{i|\boldsymbol{\mu}|^2} \left[ \mu_{\perp}^2(k_1^2 + t_{ev}^2)r_p(u_{ev}) + 0.5\mu_{\parallel}^2k_1^2r_s(u_{ev}) + 0.5\mu_{\parallel}^2t_{ev}^2r_p(u_{ev}) \right], \quad (18)$$

where  $Q$  is the quantum yield.  $u_{prop} = \sqrt{k_1^2 - t_{prop}^2}$  and  $u_{ev} = \sqrt{k_1^2 + t_{ev}^2}$ . The physical meaning of  $u$  is the wavevector component parallel to the interface ( $k_x$ ). Hence  $u_{prop}$  varies from zero to  $k_1$  and  $u_{ev}$  varies from  $k_1$  to infinity. The values of the parameter  $t$  are chosen accordingly. For the multilayer structure, the reflection coefficients are obtained by a transfer-matrix method (with the  $z$  axis perpendicular to the interfaces of the multilayer structure). Further details can be found in [17]. We see that the spectra have rather different shapes for the different samples.

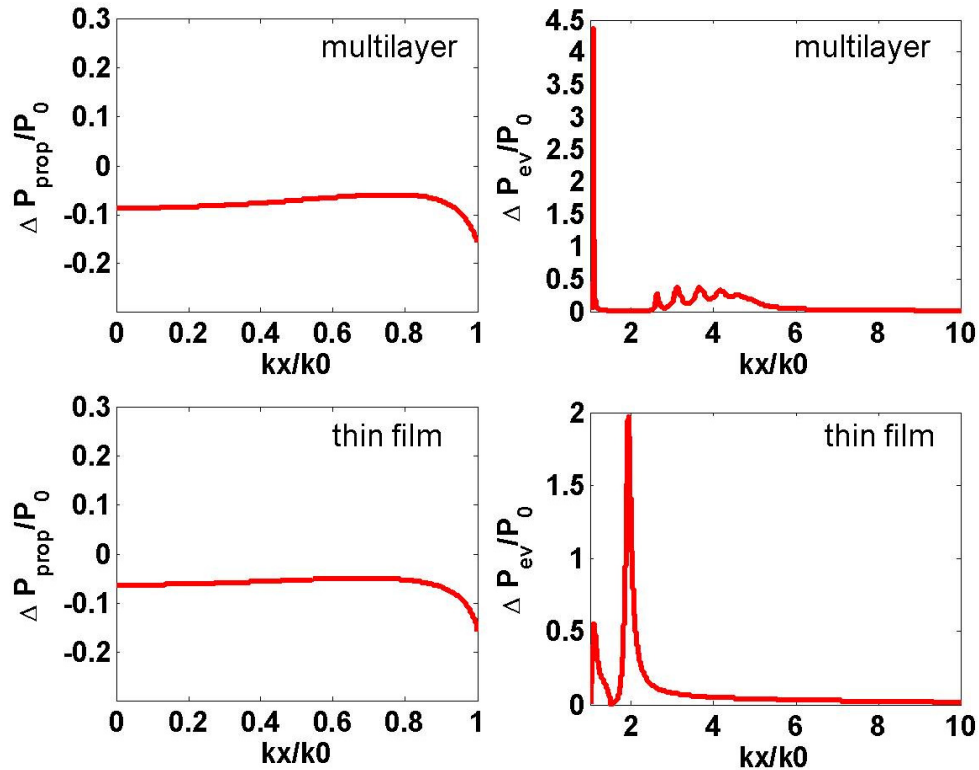


Fig. 6. Dissipated power spectra for the multilayer and thin Au film samples.

However, the total dissipated power is about the same for all samples. Thus the key difference in the effect of the substrate on the luminescence properties of the dye molecules arises from the ratio between the radiative and non-radiative parts of the dissipated power. The total decay rates obtained from our lifetime measurements as well as the radiative and non-radiative decay rates are compared in Table 6. This shows directly that both the radiative decay rates and the non-radiative decay rates are influenced by the external environment.

From Table 6 we see that the radiative decay rate near the HMM is improved over that of the thin gold sample, while the total decay rate is higher for the thin gold film relative to the HMM sample. This observation confirms that it is quite easy to obtain erroneous conclusions on radiative decay near a HMM if the analysis is based only on lifetime measurements. Purcell factors, which show the enhancement of the spontaneous emission rate relative to that of free space (in our case this is in a methanol solution), are suggested by the data in Table 6. Our maximum changes in the radiative decay rates relative to Rh800 in methanol are about 1.2 for dye molecules on glass, 1.35 for thin gold films, 1.73 for thick gold, and 2.7 for multilayer HMM samples. If we consider only the total decay rate as it was done in [21–23, 37], we would not observe this latent effect. Indeed, the total decay rate ratios are about 0.75 for glass, about 1 for thin gold films, 0.9 for thick gold films, and 1 for multilayer HMM samples. Moreover, the non-radiative decay rates also change for metal-containing samples, which in turn provide changes in the apparent quantum yield.

The overall increase in the quantum yield for thick gold is about 2.3, while for the multilayer HMM the increase is 3.5, according to our data in Table 6. In addition, the distance dependence of the effects of the HMM sample is also shown in Table 6. This dependence is qualitatively similar to the classic samples, namely the thick and thin gold films, according to the literature data and our measurements. For the smaller spacer distance, the radiative decay

rates are lower for all the samples compared to the dye-on-glass reference sample, while the non-radiative rates are higher. This makes the quantum yield strongly reduced for the 21-nm spacer case. We must recall the mechanisms of the decay process in order to understand the reason for this distance dependence. The probability of radiative and non-radiative decay of the excited molecules depends on the details of the system [2, 38]. Changes in the PDOS act to alter the radiative decay, and in addition the probability of non-radiative decay can be also changed. We have considered changes in the PDOS due to planar interfaces that mimic the experimental conditions. The coupling between the emitter and surface-plasmon polariton modes at the metal-dielectric interface increases the wavevector relative to that in free space. This makes such a mode non-radiative.

For the thin-metal sample, SPP modes can be supported at both metal-dielectric interfaces. One of these modes is an asymmetric, leaky mode that provides out-coupling of the SPP into far-field radiation [2, 5, 10, 31, 38]. The coupling between the emitters and the waveguided modes at the appropriate spacer thicknesses can sustain leaky modes if the normalized in-plane wavevector less than  $\varepsilon^{-1/2}$ , or about 0.65 for our spacer material with a dielectric constant of about 2.5. The interference of the emitted and interface reflected waves results in the PDOS changes [1]. Those experiments showed, in particular, that if the dye layer is less than  $\lambda/4$  from the metal surface, a strong distance-dependent quenching sets in. It is a common belief that the energy transfer from the excited molecules is due to electron-hole pair excitations in the metal, which is a dipole-dipole interaction in nature [2]. There are three quenching mechanisms that differ in the source of the momentum required to ensure momentum conservation. The extra momentum contributions are due to impurities and phonons in the bulk; due to scattering from the surface potential at the interface; and due to the high-wavevector components in the near field that can provide momentum conservation directly for molecules very close to the surface. If the wavelength is comparable to the characteristic length, which is in this case the mean free path of the electrons, then nonlocal effects should be taken into account as well.

The most attractive property of the hyperbolic metamaterials is the broadband and strongly enhanced Purcell factor for the fluorophore spontaneous emission. The value of the enhancement is theoretically limited only by losses [16] or finite period to wavelength ratio [16, 30]. It was shown also that the finite size of the emitter distribution can limit the HMM density of states even at zero losses [39]. Our experiments and analysis show that the main limiting factor is the effect of metamaterials on the nonradiative decay rate, which was not considered in the existing theories.

## 5. Conclusions

In conclusion, we have observed a significant increase in the radiative decay rate of dye molecules by placing them near a hyperbolic metamaterial surface relative to several control samples including thick and thin metal films that are widely studied in the literature. The described experiments determine the modification of the radiative decay, as opposed to the previous approaches which studied only changes to the total decay rate. Our experimental results show that hyperbolic multilayer metamaterials behave qualitatively similar to the metal-film samples. What is more important is that the multilayer design enables a quantitative improvement in the radiative luminescence decay. This is the first experimental verification of radiative decay rate enhancement near a multilayer hyperbolic metamaterial. This observation may form the basis of new techniques in improving the PDOS by engineering HMMs.

## Appendix

The effective-medium models used in this work are based on the Rytov approximation (Eq. 1-4). The model descriptions of the effective permittivities for all samples include the

thicknesses of all layers and fitting parameters  $A=a/d$  as well as the period  $d$ . The model names below correspond to the names used in the main manuscript text. Figures 7-9 present spectra of the x- and z- components of the effective permittivities. The model parameters were determined by matching the transmission and reflection spectra calculated with the experimental layers and the effective model layers. The spectra are shown in Figures 10-12.

Model 20:

Experimental layers: glass BK7 (0.8 mm) + (Al<sub>2</sub>O<sub>3</sub> 19nm + Au 19 nm) x 8 + epoxy (42 nm).

Effective model: glass (0.8 mm) + effective layer (275nm) + epoxy (42 nm);

x-component of  $\epsilon_{\text{eff}} = (A\epsilon_1 + (1-A)\epsilon_2)$ ; (Rytov correction with  $A = a/d = 0.5$ ,  $d = 38$  nm).

z-component: inverse average  $(\epsilon_{\text{eff}})^{-1} = A(\epsilon_2)^{-1} + B(\epsilon_1)^{-1}$ ;  $A = B = 0.5$ .

Figure 8 shows the spectra of the complex permittivities, and Fig. 11 shows the reflection and transmission spectra.

Model 24:

Experimental layers: glass BK7 (0.8 mm) + (Al<sub>2</sub>O<sub>3</sub> 19 nm + Au 19 nm) x 8 + epoxy (83 nm).

Effective model: glass (0.8 mm) + effective layer (240 nm) + epoxy (80 nm);

x-component:  $\epsilon_{\text{eff}} = (A\epsilon_1 + (1-A)\epsilon_2)$ ; (Rytov correction with  $A = a/d = 0.48$ ,  $d = 38$  nm).

z-component: inverse average  $(\epsilon_{\text{eff}})^{-1} = A(\epsilon_2)^{-1} + B(\epsilon_1)^{-1}$ ;  $A = 0.66$ ,  $B = 0.34$ ,  $\lambda_{\text{res}} = 487$  nm.

Model 23:

Experimental layers: glass BK7 (0.8 mm) + Au (19 nm) + epoxy (34 nm).

Effective model: glass (0.8 mm) + effective layer (34 nm) + epoxy (21 nm);

x-component:  $\epsilon_{\text{eff}} = (A\epsilon_1 + (1-A)\epsilon_2)$ ;  $A = a/d = 0.49$ , no Rytov correction;

z-component: inverse average:  $(\epsilon_{\text{eff}})^{-1} = A(\epsilon_2)^{-1} + B(\epsilon_1)^{-1}$ ;  $A = 1$ ,  $B = 0.5$ ;  $\lambda_{\text{res}} = 495$  nm.

Figure 7 shows the spectra of the complex permittivities, and Fig. 10 shows the reflection and transmission spectra.

Model 21:

Experimental layers: glass BK7 (0.8 mm) + Au (300 nm) + epoxy (42 nm).

Effective model: glass (0.8 mm) + Au (250 nm) + effective layer (53 nm) + epoxy (39 nm);

x-component:  $\epsilon_{\text{eff}} = (A\epsilon_1 + (1-A)\epsilon_2)$ ;  $A = a/d = 0.04$ , no Rytov correction.

z-component: inverse average:  $(\epsilon_{\text{eff}})^{-1} = A(\epsilon_2)^{-1} + B(\epsilon_1)^{-1}$ ;  $A = 1$ ,  $B = 1$ ;  $\lambda_{\text{res}} = 490$  nm.

Figure 9 shows the spectra of the complex permittivities, and Fig. 12 shows the reflection and transmission spectra.

The spectra in Figs. 10-12 below are calculated with the fitted parameters of the models as noted above and compared with the experimental reflection spectra and simulated transmission spectra using the as-fabricated design and the bulk permittivities of the components.

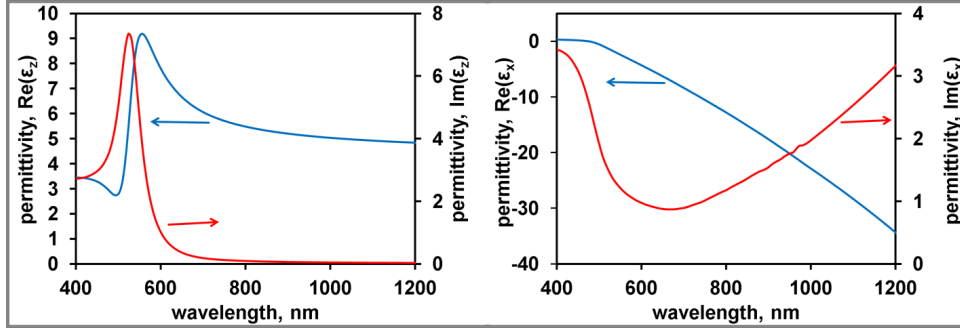


Fig. 7. Effective permittivities, z-component (left) and x-component (right) for the thin-Au sample with a 21-nm spacer, blue- real part, red - imaginary part.

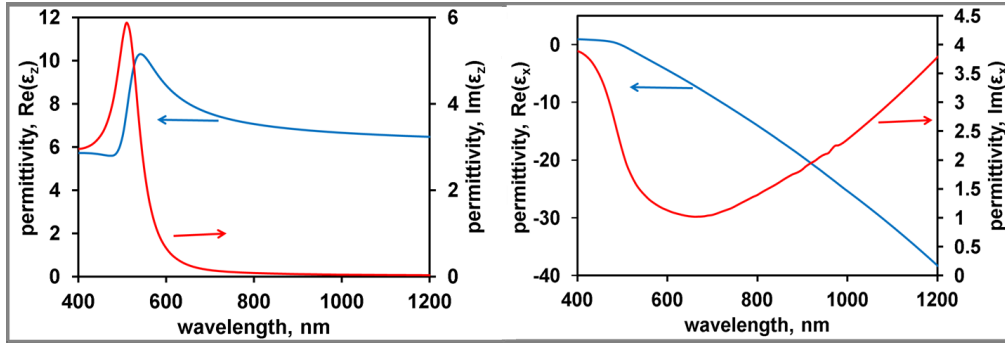


Fig. 8. Effective permittivities, z-component (left) and x-component (right) for a multilayer sample with a 21-nm spacer, blue- real part, red - imaginary part,  $\lambda_{res} = 473$  nm.

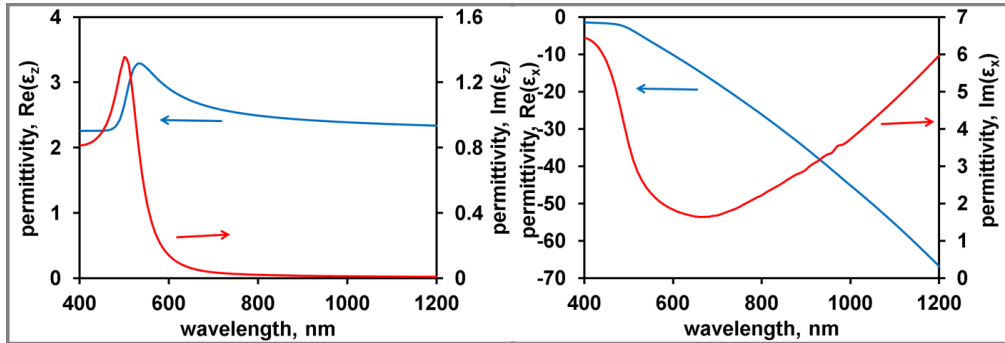


Fig. 9. Effective permittivities, z-component (left) and x-component (right) for 300-nm Au film sample with 21-nm spacer, blue- real part, red - imaginary part.

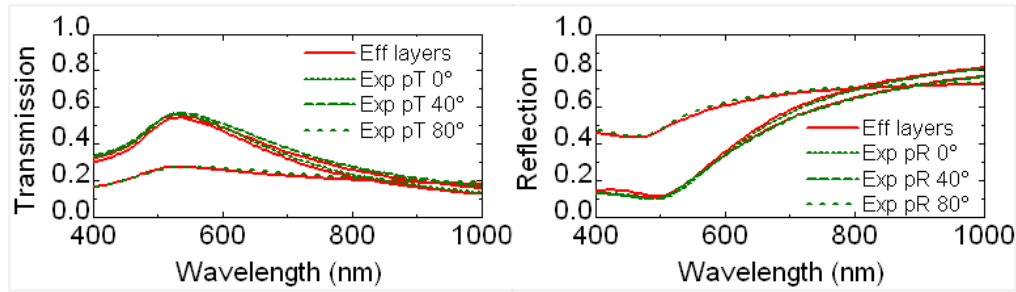


Fig. 10. Thin Au film with a 21-nm spacer: comparison of fitting results for an effective layer and experimental results.

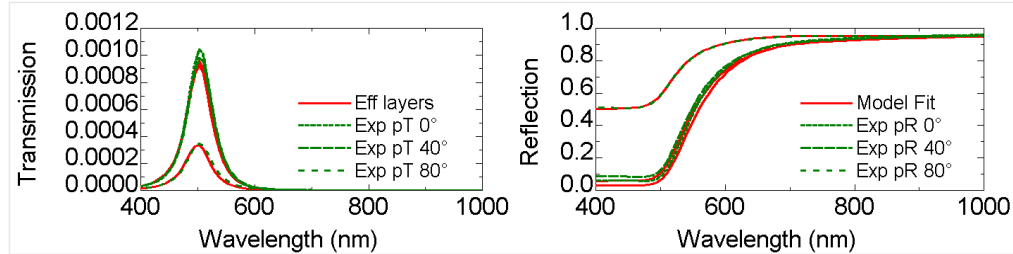


Fig. 11. Multilayer sample with 21-nm spacer: comparison of fitting results for a 275-nm effective layer at the model interface and experimental layers (19 nm Au + 19 nm alumina) x 8 + 42 nm epoxy.

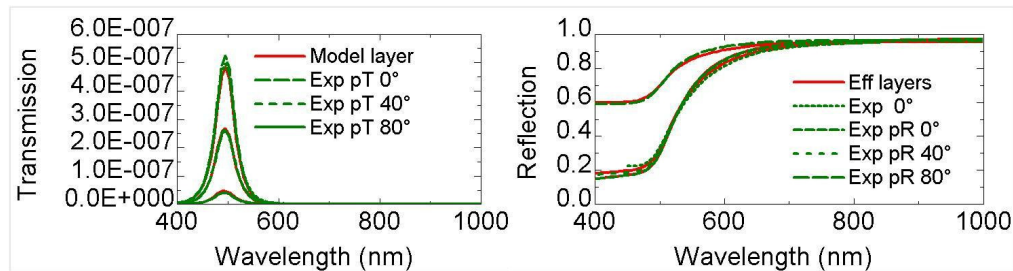


Fig. 12. Sample with a 300-nm Au film and a 21-nm spacer: comparison of fitting results for a 55-nm effective layer at the model interface and experimental results.

### Acknowledgments

This work was supported in part by ARO-MURI award 50342-PH-MUR, NSF Grant #DMR-1120923, AFOSR-MURI grant # FA9550-10-1-0264, and ONR-MURI grant N00014-10-1-0942. Z.J. wishes to acknowledge support from NSERC Discovery Grant # 402792. VPD thanks AFRL Materials & Manufacturing Directorate -Applied Metamaterials Program for partial support.